Arch Appl Mech (2014) 84:519–541
DOI 10.1007/s00419-013-0815-9

ORIGINAL

**Hui Ma · Hui Li · Heqiang Niu · Rongze Song ·
Bangchun Wen**

Numerical and experimental analysis of the first- and second-mode instability in a rotor-bearing system

Received: 29 July 2013 / Accepted: 10 December 2013 / Published online: 28 December 2013

Abstract Aiming at the oil film instability of the sliding bearing at high speeds, a rotor test rig is built to study the non-linear dynamic behaviours caused by the first- and second-mode instability. A lumped mass model (LMM) of the rotor system considering the gyroscopic effect is established, in which the graphite self-lubricating bearing and the sliding bearing are simulated by a spring–damping model and a nonlinear oil film force model based on the assumption of short bearings, respectively. Moreover, a finite element model is also established to verify the validity of the LMM. The researches focus on the effects of two loading conditions (the first- and second-mode imbalance excitation) on the onset of instability and nonlinear responses of the rotor-bearing system by using the amplitude–frequency response, spectrum cascade, vibration waveform, orbit, and Poincaré map. Finally, experiments are carried out on the test rig. Simulation and experiment all show that oil film instability can excite complicated combination frequency components about the rotating frequency and the first-/second-mode whirl/whip frequency.

Keywords Oil film instability · Rotor system · Dynamic behaviours · Combination frequency ·
The first-/second-mode whirl/whip

List of symbols

$\boldsymbol{C}$	Damping matrix of the global system
$\boldsymbol{C}_1$	Rayleigh damping matrix
$\boldsymbol{C}_2$	Bearing damping matrix
c	Bearing clearance
c_{blx}, c_{bly}	Dampings of the left bearing in x and y directions
D	Bearing diameter
E	Young's modulus
F_b	Oil film force vector of the right bearing
F_{bx5}, F_{by5}	Oil film forces of the right bearing in x and y directions
F_e	Unbalanced force vector of the rotor system
f_{bx5}, f_{by5}	Dimensionless oil film forces of the right bearing in x and y directions
f_{n1}, f_{n2}	The first- and second-mode whirl/whip frequencies
f_r	Rotating frequency
G	Gyroscopic matrix
g	Acceleration of gravity
I	Moment of inertia
$J_{di} (i = 1, 2, 3, 4, 5)$	Diametral moment of inertia about any axis perpendicular to the rotor axis

---

H. Ma (✉) · H. Li · H. Niu · R. Song · B. Wen
School of Mechanical Engineering and Automation, Northeastern University,
Shenyang, Liaoning 110819, People's Republic of China
Tel: +86-24-83684491
Fax: +86-24-83684491
E-mail: mahui_2007@163.com

$J_{pi}(i = 1, 2, 3, 4, 5)$	Polar mass moment of inertia about rotor axis
$\boldsymbol{K}$	Stiffness matrix of the global system
k_{blx}, k_{bly}	Stiffnesses of the left bearing in x and y directions
L	Bearing length
l_i	The distance between every two lumped mass points
$\boldsymbol{M}$	General mass matrix of the global system
$m_i(i = 1, 2, 3, 4, 5)$	Lumped mass
$\boldsymbol{q}$	Displacement vector
$\tilde{\boldsymbol{q}}$	Dimensionless displacement vector
u_1, u_2	Eccentricities of disc 1 and disc 2
$x_{i,}\ y_i(i = 1, 2, 3, 4, 5)$	Displacements in x and y directions
$\tilde{x}_i, \tilde{y}_i(i = 1, 2, 3, 4, 5)$	Dimensionless displacements in x and y directions
Greek symbols	
ξ_1, ξ_2	The first and second modal damping ratios
η	Lubricant viscosity
θ_{xi}, θ_{yi}	Angles of orientation about the x and y axes
τ	Dimensionless time
φ_1, φ_2	Initial phase angle of two discs
ω	Rotating speed of rotor
ω_{n1}, ω_{n2}	The first and second natural frequencies

1 Introduction

Modern rotating machineries, such as turbines, compressors, and generators, are designed in high speed, flexibility, and efficiency. In order to avoid unstable vibrations at higher operating speeds, more and more attention has been paid to self-excited vibration arising from fluid film forces. The instability caused by fluid is typically subsynchronous because it exhibits excessive vibration at the first- or second-mode whirl/whip frequency and would contribute to unstable operation, high-level vibration of the system, eventual rubbing between rotor and stator, and potential damage of the rotating machinery [1,2].

The oil film instability phenomenon has been observed firstly by Newkirk and Taylor [3], and Rao [4] gives a comprehensive overview about it. Robertson [5], Pinkus and Sternlicht [6], Morrison and Paterson [7] analysed this phenomenon and made some simple design rules. Lund [8] presented a complete methodology for the design and stability of oil film bearing. Botman [9] observed nonsynchronous vibrations at speeds above twice the critical speed in a high-speed rigid rotor-damper system. Ehrich [10] stated that rotor dynamic instabilities and self-excited vibrations generally took the form of lateral flexural vibrations at the rotor natural or critical frequency. Nikolajsen et al. [11] observed nonsynchronous vibrations in a flexible, symmetric rotor on two identical plain journal bearings supported by centralized squeeze film dampers. Muszynska [12] showed that two more thresholds of stability appeared in the first balance resonance, and the width of this stability region was directly related to the amount of rotor unbalance. In another paper, Muszynska [13] indicated that the second-mode whirl will occur when the rotational speed is higher than the third threshold of stability which has also been observed experimentally and reported from machinery filed data.

In order to better simulate the nonlinearity of sliding bearings, many researches have developed some nonlinear oil film force models. On journal bearing impedance descriptions, Childs et al. [14] proposed a nonlinear hydrodynamic force model, which could be used to analyse the stability but not to simulate the fluid-induced instability. Based on the results of a series of experiments, Muszynska et al. [15] presented a simple model of nonlinear fluid dynamic forces generated in bearings. A parameter called as the fluid average circumferential velocity ratio was used to describe the characteristic of the fluid motion as a whole. The fluid film radial stiffness, damping, and inertia effects were described by nonlinear functions of the rotor eccentricity ratio inside the bearing. Meanwhile, the model had been used to analyse anti-swirl to prevent rotor instability correctly and effectively. Mohan et al. [16] investigated squeeze film bearings supporting a centrally preloaded rigid rotor mounted in anti-friction bearings based on the short bearing approximation (small length–diameter ratio $L/D \leq 0.25$). Based on the short bearing approximation of Ocvirk [17], Capone [18,19] presented a new nonlinear oil film model and analysed the orbits of the shaft in the bearings by a model. Zhang et al. [20] proposed an effective model for unsteady oil film forces to express time-varying boundaries of the film that whirled rapidly around the journal centre. Based on Capon model, Adiletta et al. [21] studied the possible chaotic motions stemming from the nonlinear response of bearings; Jing et al. [22,23] analysed the nonlinear dynamic behaviour of bearing considering the oil whip phenomenon; de Castro et al. [24] discussed the system instability threshold influenced by the amount of unbalance, rotor arrangement form, and bearing parameters; Ding et al. [25] researched the nonstationary dynamic responses of the system during speed-up with a constant angular acceleration for a multi-bearing rotor; Cheng et al. [26] investigated nonlinear dynamic behaviours of a rotor-bearing-seal-coupled system. Rao et al. [27] presented an analytical approach based on the long bearing model and the short bearing model for nonlinear transient analysis. Chen et al. [28] studied the chaotic behaviour of a flexible rotor supported by oil film bearings with nonlinear suspension by using the long bearing approximation [29]. Based on the nonsteady nonlinear hydrodynamic forces generated by oil film [20], Ding et al. [2] studied dimension reductions of a continuous rotor system by both the standard Galerkin method and the nonlinear Galerkin method, revealed transitions or bifurcations of the rotor whirl from being synchronous to nonsynchronous as the unstable speed was exceeded, and observed the “windows” of multi-periodic motion in the regime of quasi-periodic motion.

In the turbocharger rotor-bearing system, the instability caused by full-floating ring bearings has attracted the attention of many researchers. Schweizer et al. [30] studied nonlinear oscillations of an automotive turbocharger rotor supported by full-floating ring bearings and gave a sound physical explanation of the total instability. Zhao et al. [31] analysed dynamical characteristics of a turbocharger rotor-bearing system in the different working conditions of bearing, such as span, width, gap, and so on by DyRoBeS software [32], discovered the changing rule of stability of the rotor system, and clarified the reasons of oil whirl and oil whip by the theoretical analysis of critical speed and spectrum cascades. By using the same programme (DyRoBes), Kirk et al. [33] evaluated the stability and transient response of a high-speed automotive turbocharger. Aiming at a typical turbocharger in floating bush bearings, Gunter et al. [34] analysed the linearized stability of the system for various bushing inner and outer clearance ratios. In order to make the design process much easier, Chen et al. [35] developed some computation methods for the rotordynamics of turbochargers. Tian et al. [36] discussed the effect of bearing outer clearance on the rotordynamic characteristics of a realistic turbocharger rotor over the speed range up to 3000 Hz using the run-up and run-down simulation methods. The results show that the complicated nonlinear jump phenomena with the changing bearing outer clearance can be observed. In another paper [37], they investigated the influence of unbalance on the rotordynamic characteristics of a real turbocharger rotor-floating ring-bearing system over the speed range from 0 Hz to3500 Hz using the same method. The newly obtained results evidently show the distinct phenomena brought about by the variations of the unbalance offset, which confirms that the unbalance level is a critical parameter for the system response.

In order to verify and revise the theory model, many researchers also carried out experimental study by using different forms of test rigs. Rao et al. [38] studied the effects of radial clearance, viscosity of the lubricating oil, and inlet pressure on the oil whip phenomenon of flexible rotors by experiment. For identifying the nonlinear aspects of the dynamics of a rigid unbalanced rotor on lubricated journal bearings, Adiletta et al. [39] performed an experiment to confirm the theoretical results. Through experiment, Fan et al. [40] investigated the phenomena in start-up vibration responses and presented a method for predicting instabilities of rotor systems in the coexistence of oil whip and dry whip. By a test rig, EI-Shafei et al. [41] studied the onset of instability of a flexible rotor mounted on two plain cylindrical journal bearings and analysed the influence of rotor imbalance, oil pressure, and misalignment on the initial instability speed. Sunar et al. [42] analysed the influence on fluid-induced rotor vibrations of shaft length, disc axial separation distance from the fluid film bearing, and disc imbalance through experiment and simulation. Results indicate that as the distance between the disc and the fluid film bearing increases, the instability threshold also increases, while as the shaft length increases, the instability threshold decreases, but changes in shaft length and disc location do not result in noticeable effects on the instability amplitude.

It should be noted that the above researches mostly focus on the first-mode whirl/whip. In fact, the operating speed of the rotating machinery often exceeds the second order or even higher order critical speeds to pursue higher efficiency. Thus, the second-mode whirl/whip can appear [1,13,41]. Previous studies on the second-mode whip phenomenon, the relation between the first- and second-mode whip, and the effect of unbalance on the whip forms are not sufficient. The main objective of this study is to investigate the effects of two loading conditions on the first- and second-mode whirls/whips by numerical simulation and experiment. A nonlinear oil film force model of the bearing in Ref. [18,19] is adopted due to its better accuracy and convergence. And motion equations of the system are established, which can be solved by the method of numerical integration. Amplitude-frequency response, spectrum cascade, vibration waveform, orbit, and Poincaré section are applied to analyse the nonsynchronous vibration. Meanwhile, an experiment is performed under two loading conditions to verify the simulation results qualitatively.

This paper consists of six sections. After this introduction, a model of a rotor-bearing system with two discs is provided in Sect. 2. In Sect. 3, the validity of a linear rotor-bearing system model(case 1) is examined

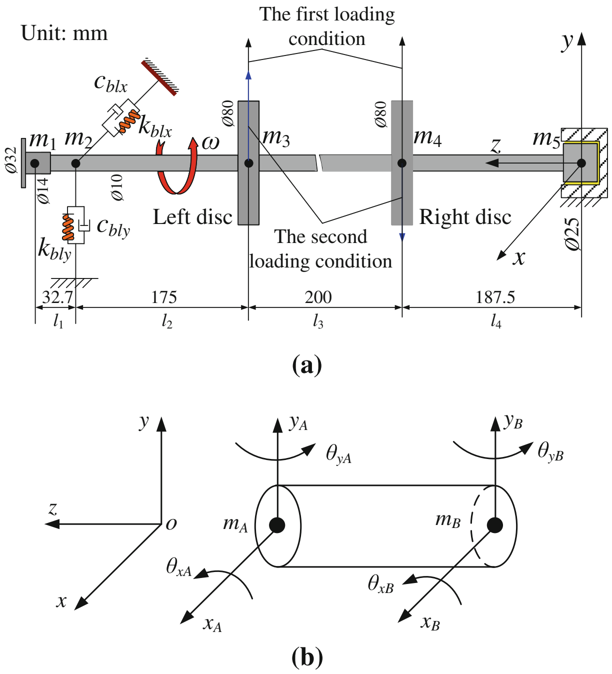

Fig. 1 Geometrical size of a rotor-bearing system and schematic of lumped mass points: **a** geometrical size, **b** schematic of lumped mass points

in Sect. 3.1; the nonlinear rotor-bearing system model is also validated in Sects. 3.2 and 3.3 (cases 2 and 3). In Sect. 4, the results of the numerical simulation under two loading conditions are provided in Sects. 4.1 and 4.2, respectively. The corresponding experiment is performed in Sect. 5. The influence of the rotating speeds is analysed under two loading condition in Sects. 5.1 and 5.2, respectively. Comparison between the simulation and experiment is performed in Sect. 5.3. Finally, some conclusions are drawn in Sect. 6.

2 Model of a rotor-bearing system with two discs

To efficiently study oil film instability problem, a mathematical model of a rotor-bearing system simulated by five lumped mass points (see Fig. 1) is simplified according to the following assumptions.

(a) The movements of the rotor in torsional and axial directions are negligible; the journals, coupling, and discs are simulated by five lumped mass points, and the corresponding points are connected with each other by massless shaft sections of lateral stiffness; each point has four (two translational and two rotational) degrees of freedom, as is shown in Fig. 1. As shown in Fig. 1a, $m_i (i = 1, 2, 3, 4, 5)$ and ω are lumped masses and rotating speed, respectively. Schematic of lumped mass points and its coordinate system are shown in Fig. 1b, where m_A and m_B denote two adjacent lumped mass points, and x_A, y_A, θ_{xA}, θ_{yA} and x_B, y_B, θ_{xB}, θ_{yB} are two translational (translation along x-axis and y-axis) and two rotational (rotation around the x-axis and y-axis) degrees of freedom about m_A and m_B, respectively.

(b) The left bearing shown in Fig. 1a is a graphite bearing, which is simulated by a spring-damping model in this paper, and the right one is a sliding bearing simulated by a nonlinear oil film force model [18,19].

In this paper, LMM is used to simulate rotor motion [43]. The mass points are generally selected at some positions, such as impellers, journals, couplings, the positions of shaft section variation, and shaft ends. The stiffnesses between adjacent lumped mass points are determined based on flexibility influence coefficient method in mechanics of materials. Based on the method [43], the motion equations of the rotor-bearing system with twenty degrees of freedom can be deduced as follows.

$$\boldsymbol{M}\ddot{\boldsymbol{q}} + (\boldsymbol{G} + \boldsymbol{C})\,\dot{\boldsymbol{q}} + \boldsymbol{K}\boldsymbol{q} = \boldsymbol{F}_e + \boldsymbol{F}_b - \boldsymbol{F}_g, \tag{1}$$

where $\boldsymbol{M}$, $\boldsymbol{G}$, $\boldsymbol{C}$, $\boldsymbol{K}$, $\boldsymbol{q}$ are mass matrix, gyroscopic matrix, damping matrix, stiffness matrix, and displacement vector of the global system (detail in the “Appendix A”).

In order to facilitate calculation and avoid excessive truncation errors, the dimensionless transformations are given as follows:

$$\tau = \omega t; \quad \tilde{\boldsymbol{q}} = \frac{\boldsymbol{q}}{c}; \quad \tilde{x}_i = \frac{x_i}{c}; \quad \tilde{y}_i = \frac{y_i}{c} \quad (i = 1, 2, 3, 4, 5)\,. \tag{2}$$

Substituting Eq. (2) into Eq. (1), the dynamic equations of the system can be rewritten in dimensionless form:

$$\omega^2 \boldsymbol{M}\ddot{\tilde{\boldsymbol{q}}} + \omega(\boldsymbol{G}+\boldsymbol{C})\dot{\tilde{\boldsymbol{q}}} + \boldsymbol{K}\tilde{\boldsymbol{q}} = \frac{\boldsymbol{F}_e + \boldsymbol{F}_b - \boldsymbol{F}_g}{c}, \tag{3}$$

$$\begin{aligned} \boldsymbol{F}_e = {} & [0, 0, 0, 0, m_3e_1\omega^2\cos(\tau+\varphi_1), 0, m_4e_2\omega^2\cos(\tau+\varphi_2), 0, 0, 0, \\ & 0, 0, 0, 0, m_3e_1\omega^2\sin(\tau+\varphi_1), 0, m_4e_2\omega^2\sin(\tau+\varphi_2), 0, 0, 0]^{\mathrm{T}}, \end{aligned} \tag{4}$$

here m_3e_1, m_4e_2, φ_1, and φ_2 denote mass eccentricities, initial phase angles of eccentricity in left and right discs, respectively.

$$\boldsymbol{F}_b = [0, 0, 0, 0, 0, 0, 0, 0, F_{bx5}, 0, 0, 0, 0, 0, 0, 0, 0, 0, F_{by5}, 0]^{\mathrm{T}}, \tag{5}$$

where F_{bx5} and F_{by5} are nonlinear oil film forces of the right bearing in x and y directions obtained by Capone model [18,19], which improves the hypothesis of π oil film by using dynamic π oil film and is appropriate for some larger length–diameter ratio conditions, such as $L/D = 0.625$ in Ref. [24]. Moreover, some literatures [24,44] also show that Capone model has a good accuracy and convergence compared with the experimental data.

Based on Capone model, nonlinear oil film forces (F_{bx5} and F_{by5}) can be expressed as follows:

$$\begin{bmatrix} F_{bx5} \\ F_{by5} \end{bmatrix} = \sigma \begin{bmatrix} f_{bx5} \\ f_{by5} \end{bmatrix}, \tag{6}$$

$$\sigma = \eta\omega\frac{D}{2}L\left(\frac{D}{2c}\right)^2\left(\frac{L}{D}\right)^2, \tag{7}$$

where η represents the viscosity of lubricating oil. L, D, and c are sliding bearing length, diameter, and radial clearance, respectively.

$$\begin{aligned} \begin{bmatrix} f_{bx5} \\ f_{by5} \end{bmatrix} = {} & \frac{\left[\left(\tilde{x}_5 - 2\dot{\tilde{y}}_5\right)^2 + \left(\tilde{y}_5 + 2\dot{\tilde{x}}_5\right)^2\right]^{\frac{1}{2}}}{1 - \tilde{x}_5^2 - \tilde{y}_5^2} \\ & \times \begin{bmatrix} 3\tilde{x}_5 V(\tilde{x}_5, \tilde{y}_5, \alpha) - \sin\alpha G(\tilde{x}_5, \tilde{y}_5, \alpha) - 2\cos\alpha S(\tilde{x}_5, \tilde{y}_5, \alpha) \\ 3\tilde{y}_5 V(\tilde{x}_5, \tilde{y}_5, \alpha) + \cos\alpha G(\tilde{x}_5, \tilde{y}_5, \alpha) - 2\sin\alpha S(\tilde{x}_5, \tilde{y}_5, \alpha) \end{bmatrix}, \end{aligned} \tag{8}$$

where the functions V, S, G, and α are, respectively, given in Eqs. (9)–(12):

$$V(\tilde{x}_5, \tilde{y}_5, \alpha) = \frac{2 + (\tilde{y}_5\cos\alpha - \tilde{x}_5\sin\alpha)\, G(\tilde{x}_5, \tilde{y}_5, \alpha)}{1 - \tilde{x}_5^2 - \tilde{y}_5^2}, \tag{9}$$

$$S(\tilde{x}_5, \tilde{y}_5, \alpha) = \frac{\tilde{x}_5\cos\alpha + \tilde{y}_5\sin\alpha}{1 - (\tilde{x}_5\cos\alpha + \tilde{y}_5\sin\alpha)^2}, \tag{10}$$

$$G(\tilde{x}_5, \tilde{y}_5, \alpha) = \frac{2}{(1 - \tilde{x}_5^2 - \tilde{y}_5^2)^{\frac{1}{2}}}\left[\frac{\pi}{2} + \arctan\frac{\tilde{y}_5\cos\alpha - \tilde{x}_5\sin\alpha}{(1 - \tilde{x}_5^2 - \tilde{y}_5^2)^{\frac{1}{2}}}\right], \tag{11}$$

$$\alpha = \arctan\left(\frac{\tilde{y}_5 + 2\dot{\tilde{x}}_5}{\tilde{x}_5 - 2\dot{\tilde{y}}_5}\right) - \frac{\pi}{2}\mathrm{sign}\left(\frac{\tilde{y}_5 + 2\dot{\tilde{x}}_5}{\tilde{x}_5 - 2\dot{\tilde{y}}_5}\right) - \frac{\pi}{2}\mathrm{sign}(\tilde{y}_5 + 2\dot{\tilde{x}}_5). \tag{12}$$

$$\boldsymbol{F}_g = [0, 0, 0, 0, 0, 0, 0, 0, 0, 0, m_1g, 0, m_2g, 0, m_3g, 0, m_4g, 0, m_5g, 0]^{\mathrm{T}}. \tag{13}$$

Substituting $\boldsymbol{M}' = \omega^2\boldsymbol{M}$, $\boldsymbol{C}' = \omega(\boldsymbol{G}+\boldsymbol{C})$, $\boldsymbol{K}' = \boldsymbol{K}$, $\boldsymbol{u} = \tilde{\boldsymbol{q}}$ and $\boldsymbol{F}' = \frac{\boldsymbol{F}_e + \boldsymbol{F}_b - \boldsymbol{F}_g}{c}$ into Eq. (3), it can be rewritten as follows.

$$\boldsymbol{M}'\ddot{\boldsymbol{u}} + \boldsymbol{C}'\dot{\boldsymbol{u}} + \boldsymbol{K}'\boldsymbol{u} = \boldsymbol{F}' \tag{14}$$

The solution of the equation of motion is obtained by using numerical methods. Here, the Newmark integration method is adopted to solve Eq. (14) because it is a robust algorithm to solve nonlinear equations in the time domain [22]. The difference format of Newmark is

$$\dot{\boldsymbol{u}}_{t+\Delta t} = \dot{\boldsymbol{u}}_t + \left[(1-\delta)\,\ddot{\boldsymbol{u}}_t + \delta\ddot{\boldsymbol{u}}_{t+\Delta t}\right]\Delta t, \tag{15}$$

$$\boldsymbol{u}_{t+\Delta t} = \boldsymbol{u}_t + \dot{\boldsymbol{u}}_t\Delta t + \left[(0.5-\alpha)\,\ddot{\boldsymbol{u}}_t + \alpha\ddot{\boldsymbol{u}}_{t+\Delta t}\right]\Delta t^2, \tag{16}$$

where δ and α are adjustable parameters depending on the required precision and stability of the numerical integration, and Δt is the integration step. The following formula can be derived from Eqs. (15) and (16).

$$\ddot{\boldsymbol{u}}_{t+\Delta t} = \frac{1}{\alpha\Delta t^2}\left(\boldsymbol{u}_{t+\Delta t} - \boldsymbol{u}_t\right) - \frac{1}{\alpha\Delta t}\dot{\boldsymbol{u}}_t - \left(\frac{1}{2\alpha} - 1\right)\ddot{\boldsymbol{u}}_t, \tag{17}$$

$$\dot{\boldsymbol{u}}_{t+\Delta t} = \frac{\delta}{\alpha\Delta t}\left(\boldsymbol{u}_{t+\Delta t} - \boldsymbol{u}_t\right) + \left(1 - \frac{\delta}{\alpha}\right)\dot{\boldsymbol{u}}_t + \Delta t\left(1 - \frac{\delta}{2\alpha}\right)\ddot{\boldsymbol{u}}_t. \tag{18}$$

Substituting Eqs. (17) and (18) into the dynamic equilibrium equations Eq. (14), it will be

$$\boldsymbol{M}'\ddot{\boldsymbol{u}}_{t+\Delta t} + \boldsymbol{C}'\dot{\boldsymbol{u}}_{t+\Delta t} + \boldsymbol{K}'\boldsymbol{u}_{t+\Delta t} = \boldsymbol{F}'_{t+\Delta t}. \tag{19}$$

Eq. (19) can be simplified as follows

$$\boldsymbol{K}^*\boldsymbol{u}_{t+\Delta t} = \boldsymbol{F}^*_{t+\Delta t}, \tag{20}$$

where

$$\boldsymbol{K}^* = \frac{1}{\alpha\Delta t^2}\boldsymbol{M}' + \frac{\delta}{\alpha\Delta t}\boldsymbol{C}' + \boldsymbol{K}', \tag{21}$$

$$\begin{aligned}\boldsymbol{F}^*_{t+\Delta t} = \boldsymbol{F}'_{t+\Delta t} &+ \left[\frac{1}{\alpha\Delta t^2}\boldsymbol{u}_t + \frac{1}{\alpha\Delta t}\dot{\boldsymbol{u}}_t + \left(\frac{1}{2\alpha} - 1\right)\ddot{\boldsymbol{u}}_t\right]\boldsymbol{M}' \\ &+ \left[\frac{\delta}{\alpha\Delta t}\boldsymbol{u}_t + \left(\frac{\delta}{\alpha} - 1\right)\dot{\boldsymbol{u}}_t + \left(\frac{\delta}{2\alpha} - 1\right)\Delta t\ddot{\boldsymbol{u}}_t\right]\boldsymbol{C}'.\end{aligned} \tag{22}$$

The solution of the equations will be unconditionally stable when the Newmark integral parameters meet the following conditions

$$\alpha = \frac{1}{4}\left(1+\gamma\right)^2, \quad \delta = \frac{1}{2} + \gamma, \quad \gamma \geq 0\,(\gamma = 0 \text{ in this paper}) \tag{23}$$

Rotating speed is selected as a control parameter, which varies with a constant step. Spectrum cascade is used to show the change of the frequency components with the control parameters. Poincaré map is adopted to indicate the nature of the system motion, which is a stroboscopic picture of motion in a phase plane, and it consists of the time series at a constant interval $T(T = 2\pi/\omega)$. The rotor orbit is used to show the moving direction of axis trace, and vibration waveform is adopted to indicate time domain features under some parameters. These will be discussed in the following sections.

Physical dimensions of the rotor system are shown in Fig. 1a. The other model parameters are listed in Table 1. Assuming that the stiffness and damping of the right bearing are the same as those of the left bearing, the first and second natural frequencies can be determined as 28.6 Hz and 105 Hz approximately.

3 Model verification

3.1 Case 1: A linear rotor-bearing system in Ref. [45]

To examine the validity of the LMM, the natural frequencies and mode shapes of a rotor-bearing system (see Fig. 2) are obtained by three models: FEM presented by Ref. [45], FEM by ANSYS software, and LMM given in this paper. In Fig. 2, the two bearings are isotropic and have a stiffness of 1MN/m in both horizontal and vertical directions, no additional stiffness to the rotational degrees of freedom, and there is no damping or cross-coupling in both bearings.

Table 1 Model parameters of the rotor-bearing system

Parameters	Value
m_1, m_2, m_3, m_4, m_5 (kg)	0.0439, 0.02343, 0.5919, 0.5919, 0.09633
J_{p1}, J_{d1} (kg m^2)	2.957×10^{-6}, 3.196×10^{-6}
J_{p2}, J_{d2}(kg m^2)	0.2929×10^{-6}, 2.966×10^{-6}
J_{p3}, J_{d3} (kg m^2)	4.735×10^{-4}, 2.478×10^{-4}
J_{p4}, J_{d4} (kg m^2)	4.735×10^{-4}, 2.478×10^{-4}
J_{p5}, J_{d5} (kg m^2)	7.526×10^{-6}, 8.780×10^{-6}
η (Pa s)	0.04
$k_{\text{blx}}, k_{\text{bly}}$ (N/m)	2×10^8, 2×10^8
$c_{\text{blx}}, c_{\text{bly}}$ (N s/m)	2×10^3, 2×10^3
c, D, L (mm)	0.3, 25, 10
ξ_1, ξ_2	0.02, 0.04
ρ (kg/m^3)	7800

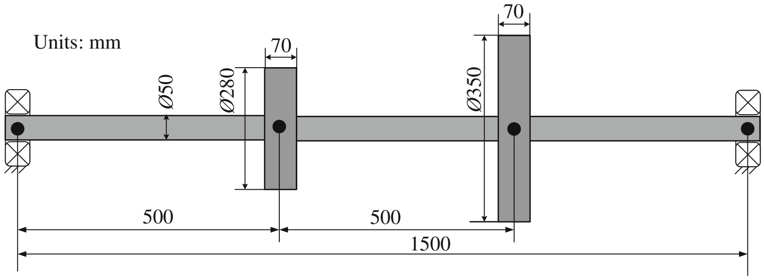

Fig. 2 Schematic diagram of a rotor-bearing system in Ref. [45]

Table 2 Natural frequencies of the rotor system by three models

Mode No.	FEM in Ref. [45]		ANSYS		LMM	
	ω_n/Hz	ω_n /Hz	ω_n/Hz	ω_n/Hz	ω_n/Hz	ω_n/Hz
	(0 rev/min)	(4,000 rev/min)	(0 rev/min)	(4,000 rev/min)	(0 rev/min)	(4,000 rev/min)
Mode 1	13.79	13.59	13.79	13.59	13.79	13.59
	13.79	13.97	13.79	13.97	13.79	13.97
Mode 2	43.66	40.07	43.65	40.24	43.53	39.95
	43.66	46.90	43.65	47.08	43.53	46.78
Mode 3	114.08	95.52	114.04	97.19	110.03	93.12
	114.08	131.63	114.04	134.76	110.03	125.71

(1) FEM in Ref. [45]
The rotor shaft is divided into seven nodes and six Timoshenko beam elements, in which gyroscopic effects are included, and the two discs are located at nodes 3 and 5, respectively.

(2) FEM by ANSYS
Based on ANSYS software, the rotor shaft is also divided into six Timoshenko beam elements by using BEAM188 element; the rigid discs are modelled as concentrated mass by using MASS21 element; two identical undamped and linear orthotropic bearings are modelled by using COMBI214 elements.

(3) LMM in this paper
The rotor system is divided into seven lumped mass points. Two discs and bearings are treated as lumped mass and superimposed upon the corresponding nodes. Every point has four degrees of freedom, including two rotational and two translational degrees of freedom.

The natural frequencies of the rotor system obtained by three models are shown in Table 2 at $\omega = 0, 4{,}000$ rev/min. Campbell diagrams and the first three mode shapes are indicated in Figs. 3 and 4, respectively. As shown in Fig. 3 and Table 2, it is clear that the first two natural frequencies by LMM are almost the same as those by other two models except that the third natural frequency is slightly different, and the first three mode shapes of FW are all same under three models (see Fig. 4).

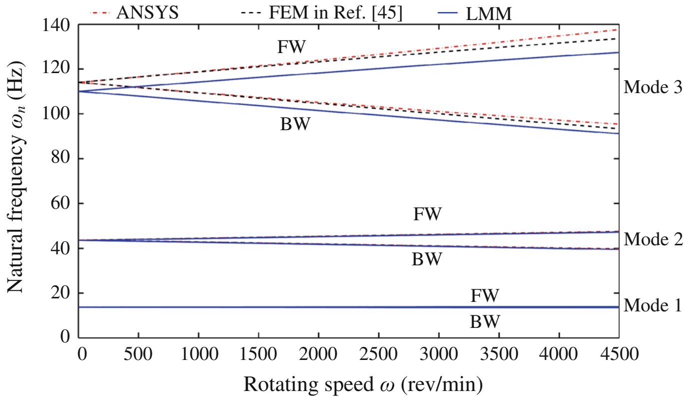

Fig. 3 Campbell diagrams of three models. Note: FW indicates forward whirl and BW backward whirl

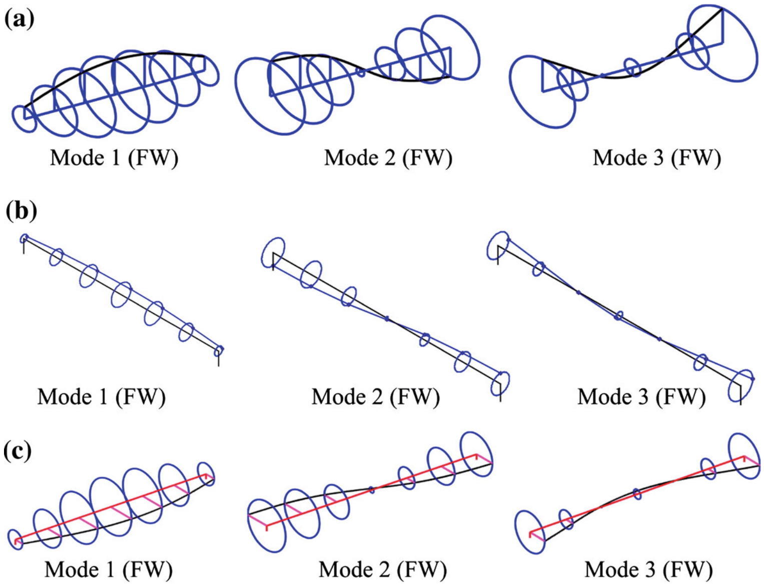

Fig. 4 Mode shapes of three models at $\omega = 4000$ rev/min: **a** Ref. [45]; **b** ANSYS; **c** LMM

3.2 Case 2: A nonlinear rotor-bearing system in Ref. [1]

The comparison of natural characteristics by three models in case 1 shows that for the linear rotor system, the LMM agrees very well with FEM. In case 2, the dynamic characteristics of a nonlinear rotor system obtained by LMM will be compared with the experimental data in Ref. [1]. Because some parameters, such as geometric parameters or mass moments of inertia of two discs, are not given in detail, they are provided approximately to make the natural frequencies approach those in Ref. [1]. The detailed model parameters are shown in Fig. 5 and Table 3.

Assuming that the two bearings in Fig. 5 are isotropic and have a stiffness of 100 MN/m in both horizontal and vertical directions, natural frequencies of the rotor system by ANSYS and LMM are shown in Table 4. It can be seen that natural frequencies by LMM are slightly larger than those by ANSYS, and the fewer nodes in LMM are the main reason for the difference.

Based on the LMM, the simulation result about a test rotor-bearing system (see Fig 4.9.17 in Ref. [1]) under the eccentricities of two discs $u_1 = u_2 = 0$ kg m (parameters in Ref. [1]) is shown in Fig. 6a. In the experiment [1], the first and second balance resonance frequencies are about 1,769 rev/min (29.5 Hz) and 4,309 rev/min (71.8 Hz), and the first and second onsets of instabilities occur at about 4,000 and 8,700 rev/min. In our simulation, the first and second balance resonance frequencies are about 1,400 and 4,600 rev/min, and the first- and second-mode instabilities appear at about 2,700 and 8,400 rev/min. For the experimental results

Table 3 Model parameters of the rotor-bearing system

Parameters	Value
m_1, m_2, m_3, m_4 (kg)	0.07, 0.7, 0.7, 0.08
J_{p1}, J_{d1} (kg m^2)	1.79×10^{-5}, 0.56×10^{-5}
J_{p2}, J_{d2} (kg m^2)	2.5193×10^{-3}, 3.6762×10^{-3}
J_{p3}, J_{d3} (kg m^2)	2.5193×10^{-3}, 3.6762×10^{-3}
J_{p4}, J_{d4} (kg m^2)	4.854×10^{-5}, 0.57×10^{-5}
η (Pa s)	0.04
c, D, L (mm)	0.152, 25, 17.8
ξ_1, ξ_2	0.02, 0.04
ρ (kg/m^3)	7850

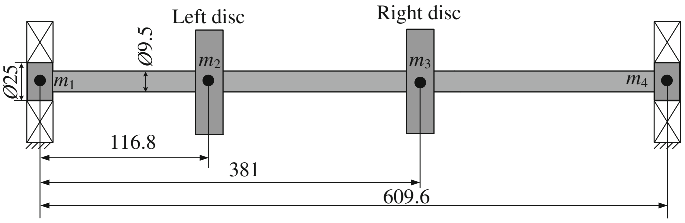

Fig. 5 Schematic diagram of a rotor-bearing system in Ref. [1]

Table 4 Natural frequencies of the rotor system under two models

Mode No.	ANSYS		LMM	
	ω_n/Hz (0 rev/min)	ω_n/Hz (4,000 rev/min)	ω_n/Hz (0 rev/min)	ω_n/Hz (4,000 rev/min)
Mode 1	20.82	18.29	22.71	19.64
	20.82	23.35	22.71	25.62
Mode 2	72.72	66.59	77.26	70.35
	72.72	76.59	77.26	81.42

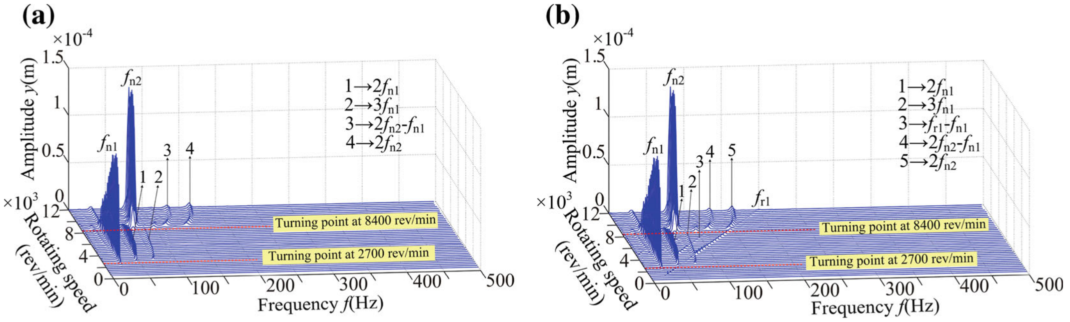

Fig. 6 Simulations of a rotor-bearing system in Ref. [1]: **a** $u_1 = u_2 = 0$ kg m; **b** $u_1 = u_2 = 7 \times 10^{-5}$ kg m and $\varphi_1 = \varphi_2 = 0°$

in Ref. [1], the rotating frequency (f_r) can be easily observed, namely unbalance is inevitable, so another simulation is performed considering $u_1 = u_2 = 7 \times 10^{-5}$ kg m, $\varphi_1 = \varphi_2 = 0°$ (assumed parameters), as is shown in Fig. 6b. Compared with the test data, the experiment and simulation all show that the first- or second-mode whip appears at about double the first or second critical speed. So to some extent, our simulation results are in good agreement with those of practical measurement in Ref. [1].

3.3 Case 3: A nonlinear rotor-bearing system presented in this paper

In case 3, simulation results of a nonlinear rotor-bearing system (see Fig. 1a) by LMM are compared with those by FEM (the details about the FEM of the rotor system can be obtained in Ref. [46], and the nonlinear

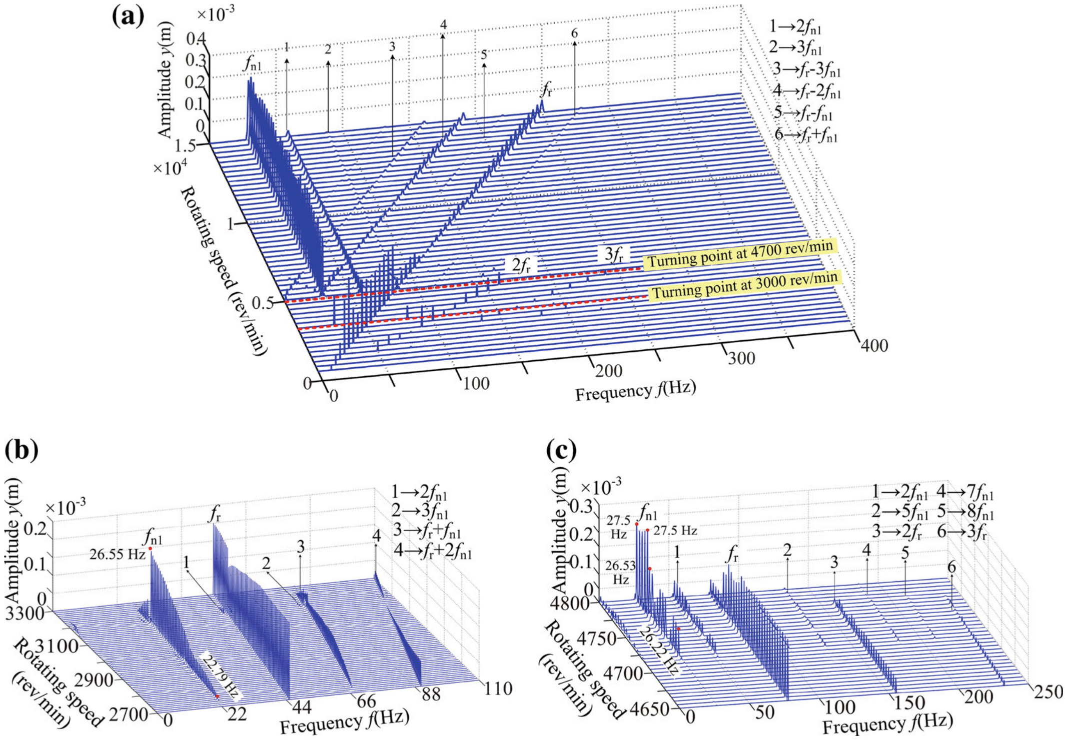

Fig. 7 Vibration response of the bearing rotor system: **a** spectrum cascade; **b** elaborate spectrum cascade in the range of $\omega \in [2700, 3300]$ rev/min; **c** elaborate spectrum cascade in the range of $\omega \in [4650, 4800]$ rev/min

oil film model is the same as that in LMM) to examine the validity of the former. In this paper, only vibration responses of the right journal in y direction (lumped mass point 5) are shown. Assuming that the eccentricities of two discs $u_1 = u_2 = 1.1838 \times 10^{-4}$ kg m are in-phase, spectrum cascade of the rotor system is shown in Fig. 7a. The figure shows that when the rotating speed approaches about double the first natural frequency about 3,000 rev/min, the half-speed oil whirl frequency reaches the value of the first balance resonance and disappears at 3,300 rev/min; synchronous motion appears in the ranges of $\omega \in$[3300, 4700] rev/min; oil whip appears at 4,700 rev/min, and the whip frequency remains close to the first critical speed; the amplitude of oil whip is much higher than that of synchronous vibration. In addition, the frequency components of the system caused by oil whip include the first-mode whip frequency f_{n1}, rotating frequency f_{r} and combination frequencies of both, such as $2f_{\mathrm{n1}}$, f_{r}–$3f_{\mathrm{n1}}$, $f_{\mathrm{r}} + f_{\mathrm{n1}}$, etc.

Elaborate spectrum cascades in the ranges of $\omega \in [2700, 3300]$ rev/min and $\omega \in [4650, 4800]$ rev/min are shown in Fig. 7b, c, respectively. Figure 7b describes the process from oil whirl to oil whip. The whirl frequency is about 22.79 Hz when $\omega = 2730$ rev/min and oil whip locks up at the first critical speed and lasts for a short time in the ranges of $\omega \in [3200, 3250]$ rev/min. The similar process from synchronous motion through oil whirl to oil whip can be observed in Fig. 7c.

FEM of the rotor system shown in Fig. 1a is established by Timoshenko beam where the model includes 26 elements and 27 nodes (see Ref. [46]). Nodes 4, 11, 19, and 26 denote graphite bearing (left bearing), left disc, right disc, and journal bearing (right bearing), respectively. The applied loadings at two discs are the same as those in LMM. Based on the FEM, the spectrum cascade and elaborate spectrum cascades of the rotor system (right journal) are shown in Fig. 8. Compared with the vibration responses by LMM, the frequency components by FEM remain largely unchanged except that the onset of the second instability speed reduces to 4,500 rev/min. Moreover, the elaborate spectrum cascades by LMM also agree basically with those obtained by FEM.

Above, comparison analysis of two models indicates that LMM can replace FEM to simulate the vibration responses of this rotor-bearing system and its computation efficiency is higher. So, in the next sections, LMM will be adopted to carry out numerical simulation.

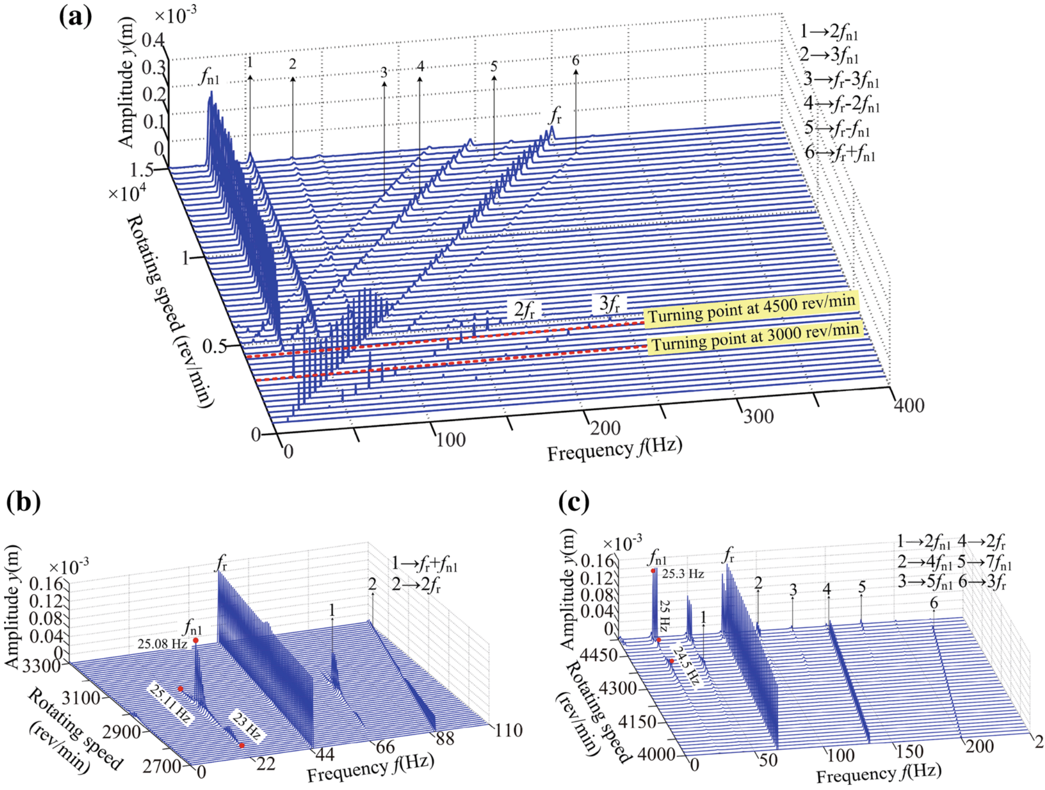

Fig. 8 Vibration response of the bearing rotor system (node 26): **a** spectrum cascade; **b** elaborate spectrum cascade in the range of $\omega \in [2700, 3300]$ rev/min; **c** elaborate spectrum cascade in the range of $\omega \in [4000, 4525]$ rev/min

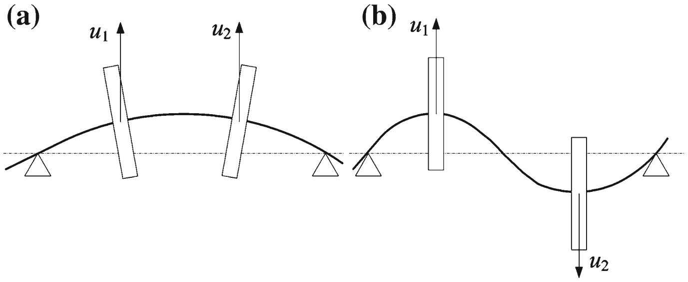

Fig. 9 The schematic diagram of two loading conditions: **a** condition 1: in-phase eccentricities of two discs; **b** condition 2: out-of-phase eccentricities of two discs

4 Results of the numerical simulation

The two unbalanced loading conditions (the first- and second-mode imbalance excitation) are determined by the modal shape of the system, as are shown in Fig. 9. In the figure, u_1 and u_2 denote the eccentricities of discs 1 and 2, respectively. For the first loading condition, $u_1 = u_2 = 1.1838 \times 10^{-4}$ kg m are in-phase, and for the second loading condition, the eccentricities are the same as the former but out-of-phase. The schematic diagram of two loading forms in the rotor-bearing system can be observed in Fig. 1a.

Assuming that the right bearing is simulated by the same spring-damping model as the left bearing, amplitude-frequency responses of the right disc (lumped mass point 4) under two loading conditions, and the first two mode shapes are given in Figs. 10 and 11, respectively. The first and second peeks of amplitude appear at about 1,750 and 6,350 rev/min, respectively, which match up with the first and second natural frequencies of 1,716 rev/min (28.6 Hz) and 6,300 rev/min (105 Hz) very well. It also shows that our calculation method is effective on the other hand.

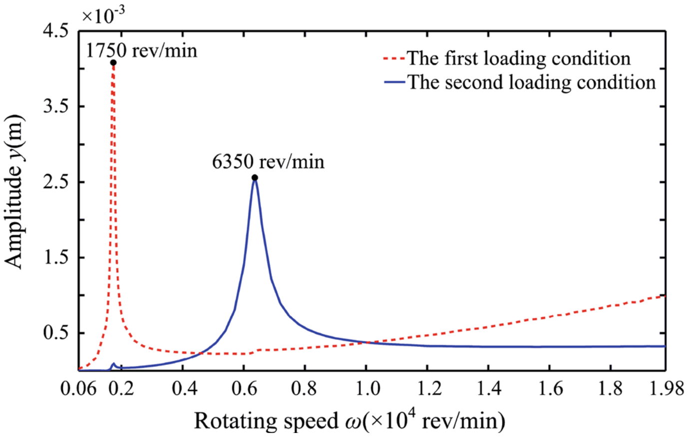

Fig. 10 Amplitude-frequency responses under two loading conditions

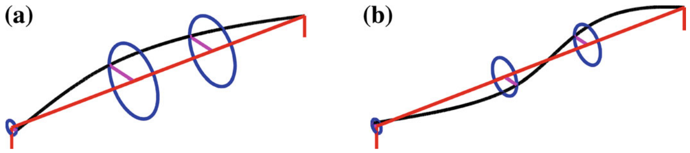

Fig. 11 Mode shapes of LMM at $\omega = 0\,\text{rev/min}$: **a** Mode 1 (28.6 Hz); **b** Mode 2 (105 Hz)

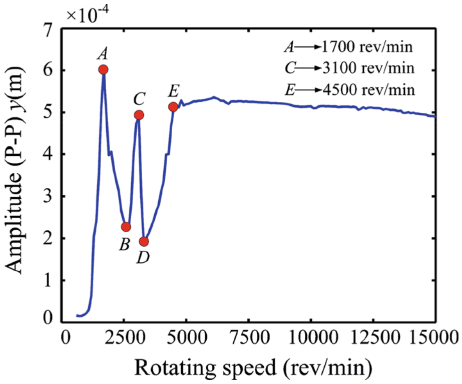

Fig. 12 Amplitude-frequency response of the rotor-bearing system under the first loading condition

4.1 The first loading condition

Amplitude-frequency response of the rotor system under the first loading condition (see Fig. 12, where 'P–P' denotes peak-to-peak value) displays the following dynamic phenomena:

(1) When the rotating speed of the journal is at about the first critical speed, resonance occurs as shown by point A (about 1,700 rev/min).
(2) After the first critical speed, the vibration amplitude decreases suddenly to point B.
(3) Further increasing speed results in a rapid increase in the vibration amplitude up to a larger magnitude at point C (about 3,100 rev/min), which is caused by the first-mode whip and corresponds to the first turning point at 3,000 rev/min in Fig. 7a.
(4) The first-mode whip lasts a short time and disappears at point D.
(5) The first-mode whip appears again at point E (about 4,500 rev/min) with increasing speed, which corresponds to the second turning point at 4,700 rev/min in Fig. 7a.

Vibration waveforms of the rotor system, rotor orbits, and Poincaré maps at constant speeds are shown in Figs. 13 and 14, respectively. The system shows quasi-periodic motion at 2,800 rev/min that is similar to period-two, period-one motion at 4,400 rev/min, and quasi-periodic motion at 6,000 rev/min, which can be

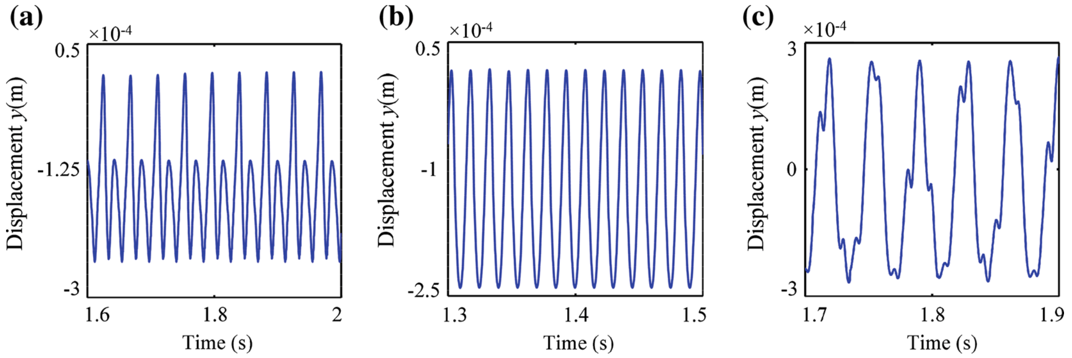

Fig. 13 Vibration waveforms of the rotor system under the first loading condition: **a** 2,800 rev/min, **b** 4,400 rev/min, **c** 6,000 rev/min

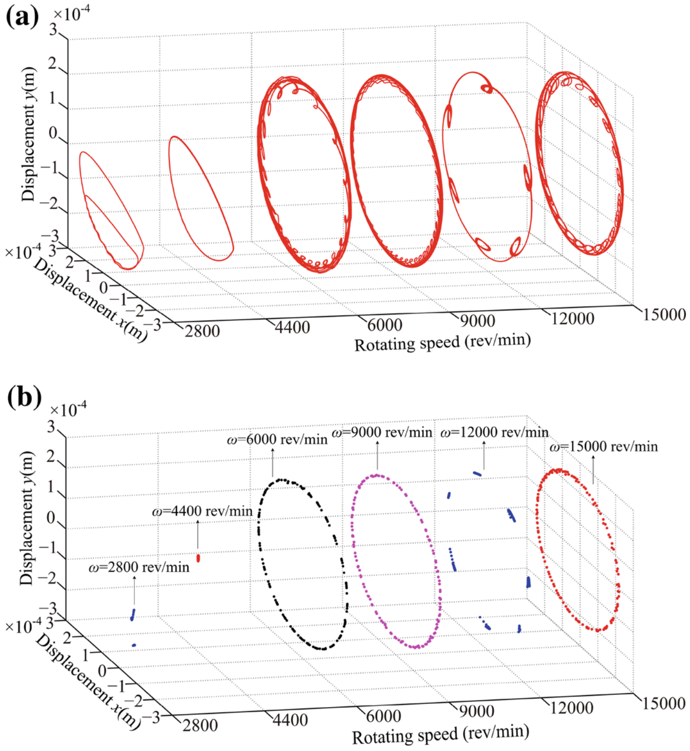

Fig. 14 Rotor orbits and Poincaré maps of the rotor system under the first loading condition: **a** rotor orbits; **b** Poincaré maps

determined by a closed circle in Poincaré maps. Similarly, the system motion is quasi-periodic at 9,000 rev/min, 12,000 and 15,000 rev/min by observing the rotor orbits and Poincaré maps at these speeds.

4.2 The second loading condition

Vibration responses of the bearing rotor system are shown in Fig. 15 under the second loading condition, which exhibits the following dynamic phenomena.

(1) There are four larger peak points in amplitude-frequency response (see Fig. 15a). The first peak (point A) corresponds to the first critical speed (about 1,300 rev/min); the second peak (point B) shows double the first critical speed (about 3,200 rev/min, here the first-mode whip appears and lasts for a short time); the third peak (point C) also indicates the first-mode instability (about 3,800 rev/min), and the fourth peak (point D) displays the second critical speed (about 6,300 rev/min).

(2) The corresponding spectrum cascade of Fig. 15a (see Fig. 15b) shows that when the rotating speed approaches about double the first natural frequency about 3,000 rev/min, the half-speed oil whirl fre-

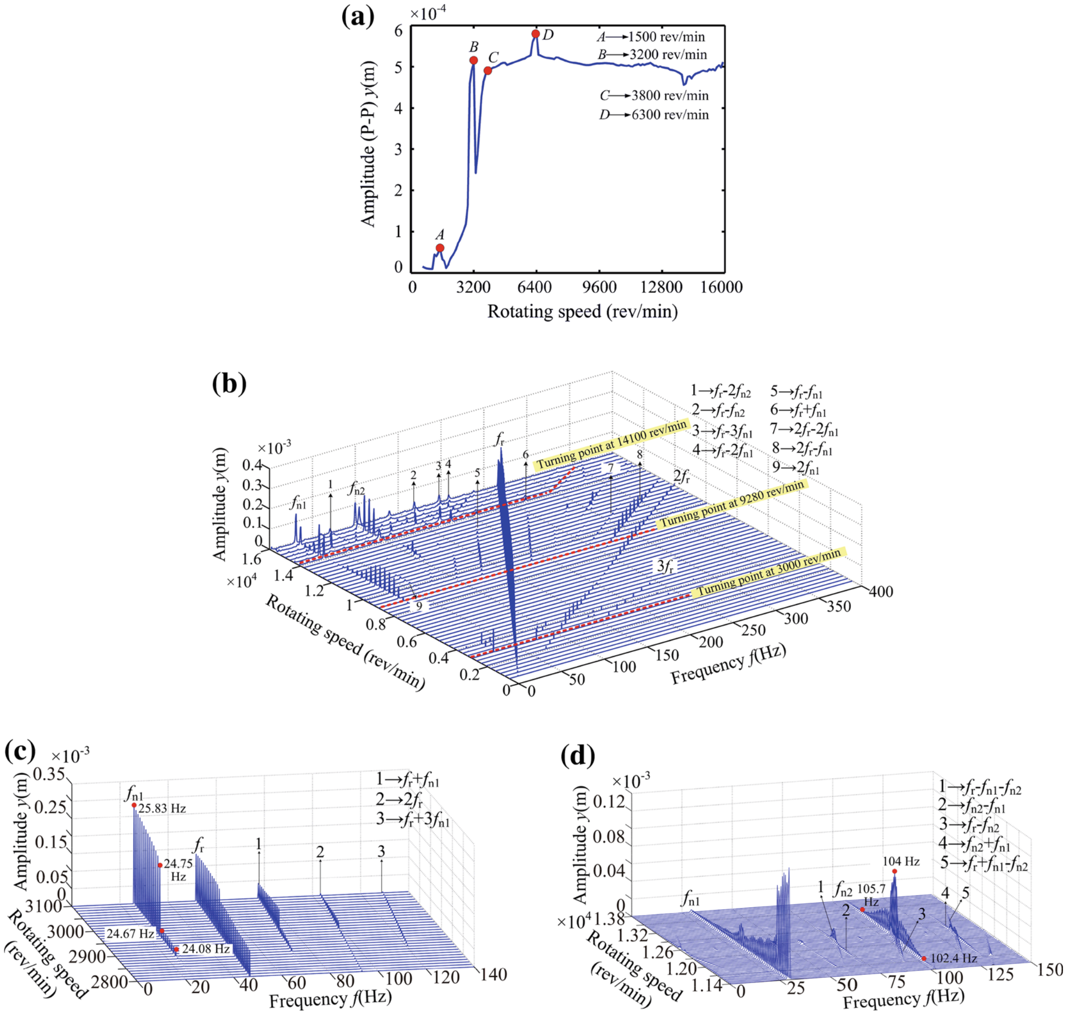

Fig. 15 Vibration responses of the bearing rotor system under the second loading condition: **a** amplitude-frequency response; **b** spectrum cascade in y direction; **c** elaborate spectrum cascade in the range of $\omega \in [2800, 3100]$ rev/min; **d** elaborate spectrum cascade in the range of $\omega \in [11400, 13800]$ rev/min

quency reaches the value of the first balance resonance and disappears at 4,300 rev/min; synchronous motion appears at $\omega \in [4300, 9280]$ rev/min; the first-mode whip appears at 9,280 rev/min, and the whip frequency remains close to the first critical speed of the rotor; the second-mode instability appears at $\omega \in [12300, 13200]$ rev/min, and the amplitude of f_{n2} increases sharply when $\omega \geq 14100$ rev/min. The frequency components of the system in different rotating ranges include complicated combination frequency components about f_{r}, f_{n1}, and f_{n2}, such as $f_{\mathrm{r}}–3f_{\mathrm{n1}}$, $f_{\mathrm{r}}–2f_{\mathrm{n1}}$, $f_{\mathrm{r}} - f_{\mathrm{n1}}$, etc.

(3) Elaborate spectrum cascades in the ranges of $\omega \in [2800, 3100]$ rev/min and $\omega \in [11400, 13800]$ rev/min can be found in Fig. 15c, d. The system motion is synchronous in the range of $\omega \in [2800, 2900]$ rev/min. Oil whirl appears in the range of $\omega \in [2890, 2960]$ rev/min and oil whip in the range of $\omega \in [2960, 3100]$ rev/min (see Fig. 15c). The process from synchronous motion through the second oil whirl to the second oil whip is shown in Fig. 15d, where some combination frequency components about f_{r}, f_{n1}, and f_{n2} can be observed such as $f_{\mathrm{r}} - f_{\mathrm{n1}} - f_{\mathrm{n2}}$, $f_{\mathrm{n2}} - f_{\mathrm{n1}}$, and $f_{\mathrm{n2}} + f_{\mathrm{n1}}$, which is similar to the experimental results (Fig. 21 in reference [24]).

Vibration waveforms of the rotor system, rotor orbits, and Poincaré maps at constant speeds are shown in Figs. 16 and 17, respectively. The system shows quasi-periodic motion at 3,200 rev/min, period-one motion at 7,000 rev/min, and quasi-periodic motion at 10,000, 12,400, 14,400 and 15,900 rev/min, which can be deduced by a closed circle in Poincaré maps.

Some different dynamic behaviours under two loading conditions can be summed as follows:

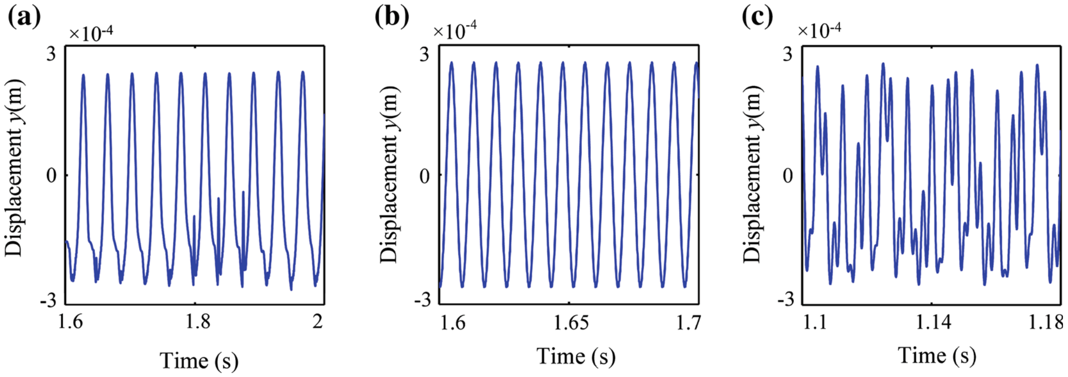

Fig. 16 Vibration waveforms of the bearing rotor system (lumped mass point 5) under the second loading condition: **a** 3,200 rev/min; **b** 7,000 rev/min; **c** 15,900 rev/min

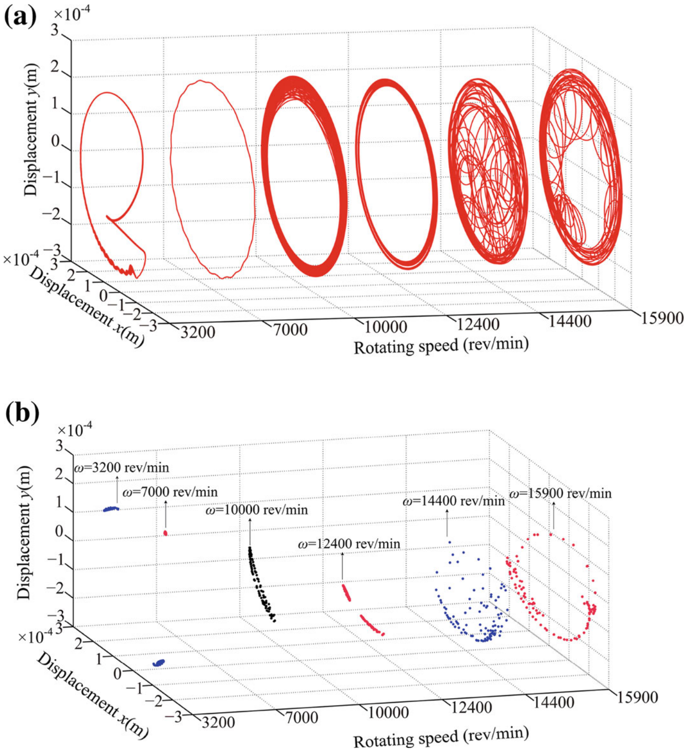

Fig. 17 Rotor orbits and Poincaré maps of the rotor system under the second loading condition: **a** rotor orbits, **b** Poincaré maps

(1) The first- and second-mode whirls/whips all occur, and combination frequencies about f_r, f_{n1}, and f_{n2} can be observed under the second loading condition. However, only the first-mode whirl/whip occurs and complicated combination frequency components about f_r and f_{n1} can be observed under the first loading condition.

(2) Stable regions increase under the second loading condition compared with those under the first loading condition.

5 Experimental results

In order to verify the simulation results, the corresponding experimental studies are conducted in a simple test rig (see Fig. 18). The rotor is driven by a small motor with frequency control. Four eddy current transducers are applied to measure the vibration displacements of the rotor in both horizontal and vertical directions (x

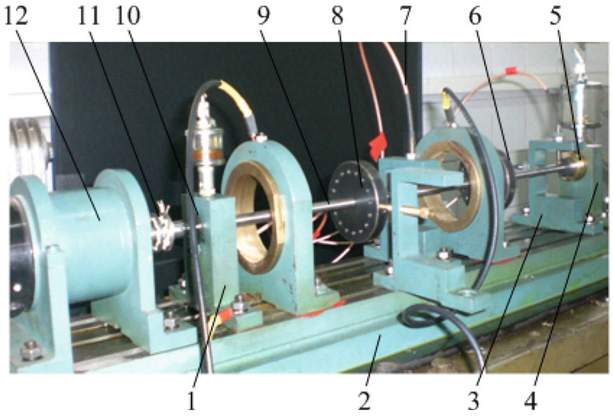

Fig. 18 A test rig of a rotor system with two discs: *1* left bearing pedestal; *2* platform; *3* sensor holder; *4* right bearing pedestal; *5* sliding bearing (right bearing); *6* right disc; *7* eddy current transducer; *8* left disc; *9* shaft; *10* graphite bearing (left bearing); *11* coupling; *12* motor

and *y* directions), and the sample frequency is 2000 Hz. Twenty-four 4 mm diameter screwed holes are drilled in each disc on a 60-mm diameter circle. By adding and reducing screws in two discs, two loading conditions shown in Fig. 9 can be conveniently simulated.

5.1 The first loading condition

Measured vibration responses of the rotor system under the first loading condition (see Fig. 19) show the following dynamic phenomena.

(1) Amplitude-frequency response of the rotor near the right journal is shown in Fig. 19a. The first peak appears at point *A*, which corresponds to the first critical speed (1,641 rev/min). The second peak at point *B* corresponds to the second critical speed (about 5,625 rev/min). The onset of the slight first-mode whip appears at about 7,148 rev/min (see point *C*), which corresponds to the second turning point at about 6,914 rev/min in Fig. 19b. The serious first-mode whip appears at point *D* (about 11,720 rev/min).

(2) The spectrum cascade corresponding to Fig. 19a (see Fig. 19b) shows some combination frequencies about f_r and f_n1, such as f_n1, $2f_\mathrm{n1}$, etc. Three turning points (2,800, 6,914 and 11,952 rev/min) about the first-mode whip can be observed. The slight first-mode whips occur at 2,800 and 6,914 rev/min and last for a shorter time, and the serious whip with steady state appears when $\omega \geq 11952$ rev/min.

Vibration waveforms of the rotor system, amplitude spectra, and rotor orbits at constant speeds are shown in Figs. 20 and 21, respectively. The system shows quasi-periodic motion at 3,984 rev/min, which can be determined by the appearance of irreducible frequency components, such as f_n1 and $f_\mathrm{r} + f_\mathrm{n1}$. System motion is period-one at 4,600 rev/min and quasi-periodic at 12,600 rev/min. The rotor orbits show two twining circles at 3,984 rev/min and multiple twining circles at 12,600 rev/min.

5.2 The second loading condition

Measured vibration responses of the rotor system under the second loading condition are shown in Fig. 22, which indicates some complicated dynamic behaviours compared with those in Fig. 19.

(1) Amplitude-frequency response (see Fig. 22a) shows more peak points, which appear at 1,758 rev/min (near the first critical speed), 2,813, 3,750 and 5,508 rev/min (the second critical speed), 7,148, 9,492 and 11,840 rev/min.

(2) Turning points about the change of the frequency components are marked in the spectrum cascade (see Fig. 22b). In the figure, the combination frequencies about f_n1, f_n2, and f_r, four turning points (2,700, 6,914, 8,438 and 11,719 rev/min), can be observed. The first-mode whip appears firstly at 2,700 rev/min and disappears at about 4,453 rev/min. It is replaced by the synchronous motion until 6,914 rev/min and resumes from 6914 to 8,438 rev/min. Then, the second-mode whip appears at 8,438 rev/min and

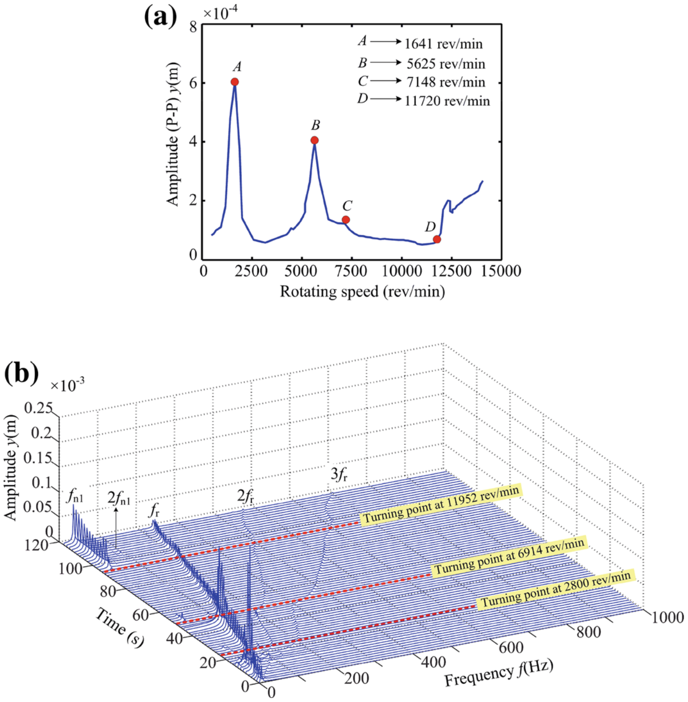

Fig. 19 Measured vibration responses of the rotor-bearing system under the first loading condition: **a** amplitude-frequency response **b** spectrum cascade in *y* direction

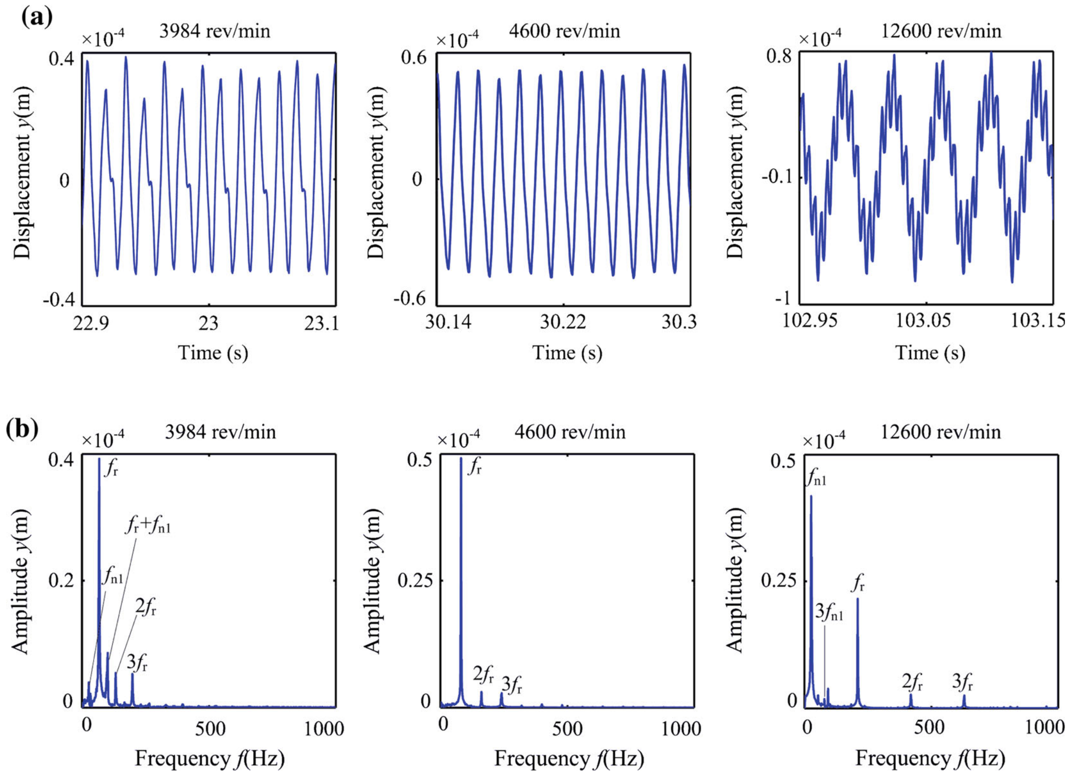

Fig. 20 Vibration responses of the rotor-bearing system at 3,984, 4,600, and 12,600 rev/min under the first loading condition: **a** vibration waveforms; **b** amplitude spectra

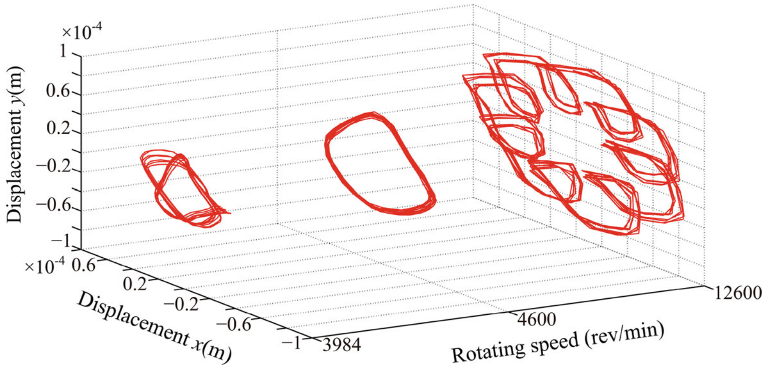

Fig. 21 Rotor orbits under the first loading condition

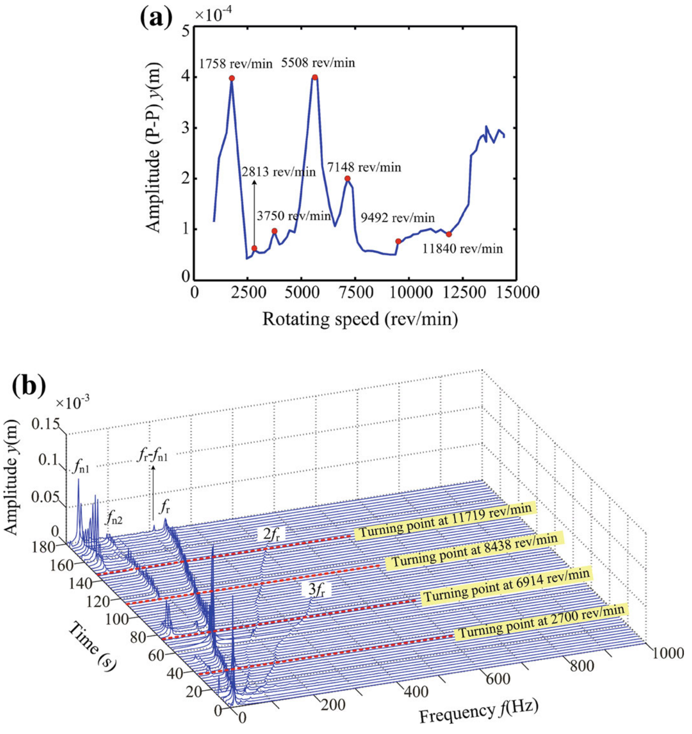

Fig. 22 Measured vibration response of the bearing rotor system under the second loading condition: **a** amplitude-frequency response; **b** spectrum cascade in y direction

continues until the last. Besides, the first-mode whip appears for the third time at 11,719 rev/min, and the amplitude of the first-mode whip increases sharply; meanwhile, the amplitude of the second-mode whip greatly reduces.

Vibration waveforms of the rotor system, amplitude spectra, and rotor orbits at constant speeds are shown in Figs. 23 and 24, respectively. The system motions are all quasi-periodic at 3,378, 11,076 and 13,150 rev/min. Combination frequency components can be observed in amplitude spectrum (see Fig. 23b). The rotor orbits show multiple twining circles at three constant rotating speeds.

5.3 Comparison of simulation and test results

For the first loading condition, the simulation and experiment all show that the first-mode whip appears at about double the first critical speed, and complicated combination frequency components about f_r and f_{n1} can be observed. However, the synchronous motion regions have bigger differences and the detailed stable regions,

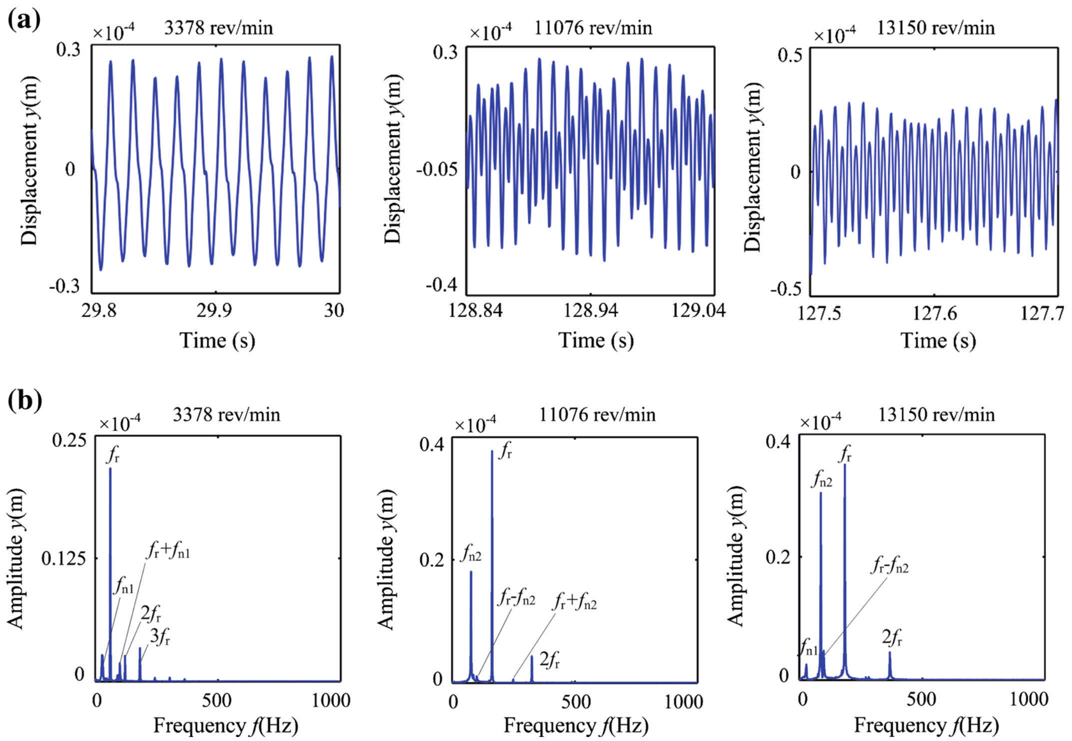

Fig. 23 Vibration waveforms and amplitude spectra of the bearing rotor system at 3,378, 11,076, and 13,150 rev/min under the second loading condition: **a** vibration waveforms; **b** amplitude spectra

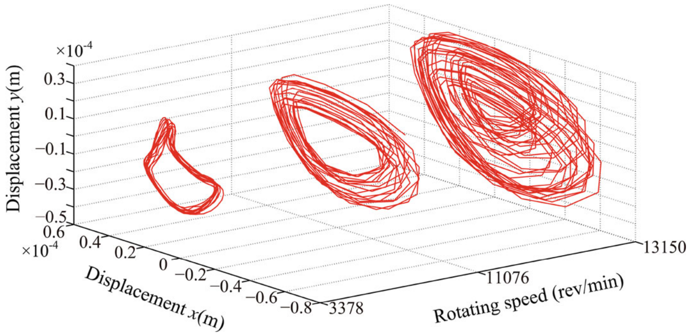

Fig. 24 Rotor orbits under the second loading condition

frequency features about simulation, and experiment are listed in Table 5. For the second loading condition, the onset of the first-mode whip (3,000 rev/min) through simulation is similar to that (2,700 rev/min) through the experiment measurement and the instability regions are also consistent with those of experimental results. The threshold speed of instability obtained by numerical simulation is greater than those by experimental measurement.

6 Conclusions

In this paper, a model considering nonlinear oil film forces is put forward to analyse the first- and second-mode instability in a rotor-bearing system. The effectiveness of the lumped mass model (LMM) is validated based on three cases. Two loading conditions are determined based on API Standard 617, and vibration responses of the system are calculated under two loading conditions by using Newmark numerical integration method. Finally, the simulation results are validated by experiments. The conclusions drawn from the study can be summarized as follows:

Table 5 Frequency feature comparison of simulation and experiment

Conditions	Rotating speed (rev/min)	Frequency features
Simulation		
The first loading condition	$600 \le \omega < 2730$	$f_r, 2f_r$ (synchronous motion)
	$2730 \le \omega \le 3250$	$f_r, f_{n1}, 2f_r, 3f_r$
	$3250 < \omega < 4720$	$f_r, 2f_r$ (synchronous motion)
	$4720 \le \omega \le 15000$	$f_r, f_{n1}, 2f_{n1}, f_r-3f_{n1}, f_r-2f_{n1}, f_r-f_{n1}, f_r+f_{n1}$
The second loading condition	$600 \le \omega < 2890$	$f_r, 2f_r$ (synchronous motion)
	$2890 \le \omega \le 4300$	$f_r, f_{n1}, 2f_r, 3f_r$
	$4300 < \omega < 9280$	$f_r, 2f_r$ (synchronous motion)
	$9280 \le \omega < 11700$	$f_{n1}, f_{n1}, f_r-3f_{n1}, f_r-2f_{n1}, f_r-f_{n1}, f_r, f_r+f_{n1}, f_r+2f_{n1}$
	$11700 \le \omega \le 13800$	f_{n1}, f_{n2}, f_r
	$13800 < \omega < 14100$	f_r (synchronous motion)
	$14100 \le \omega \le 16000$	$f_{n1}, 2f_{n1}, f_r-3f_{n1}, f_r-2f_{n1}, f_r-2f_{n2}, f_r-f_{n2}, f_{n2}, f_r$
Experiment		
The first loading condition	$600 \le \omega < 2800$	$f_r, 2f_r, 3f_r$ (synchronous motion)
	$2800 \le \omega \le 4453$	$f_r, f_{n1}, f_r+f_{n1}, 2f_r, 3f_r$
	$4453 < \omega < 6914$	$f_r, 2f_r, 3f_r$ (synchronous motion)
	$6914 \le \omega \le 7615$	$f_{n1}, f_r, 2f_r, 3f_r$
	$7615 < \omega < 11952$	$f_r, 2f_r, 3f_r$ (synchronous motion)
	$11952 \le \omega \le 14064$	$f_{n1}, 2f_{n1}, f_r, 2f_r, 3f_r$
The second loading condition	$600 \le \omega < 2700$	$f_r, 2f_r, 3f_r$ (synchronous motion)
	$2700 \le \omega \le 4688$	$f_r, f_{n1}, f_r+f_{n1}, 2f_r, 3f_r$
	$4688 < \omega < 6914$	$f_r, 2f_r, 3f_r$ (synchronous motion)
	$6914 \le \omega \le 7620$	$f_{n1}, 2f_{n1}, f_r-f_{n1}, f_r, 2f_r, 3f_r$
	$7620 < \omega < 8438$	$f_r, 2f_r, 3f_r$ (synchronous motion)
	$8438 \le \omega \le 11719$	$f_{n2}, f_r, 2f_r$
	$11719 < \omega \le 14178$	f_{n1}, f_{n2}, f_r

(1) Natural characteristics calculated by LMM agree well with those by FEM for the linear rotor system. The dynamic characteristics of a nonlinear rotor system are in good agreement with those of practical measurement in Ref. [1]; furthermore, the vibration responses of our rotor-bearing system calculated by LMM and FEM match well.

(2) The simulations reveal that complicated combination frequencies appear under two loading conditions. Under the first loading condition, the frequency components include rotating frequency (f_r), the first-mode whirl/whip frequency (f_{n1}), and combination frequencies of both. Under the second loading condition, the frequency components are more complicated, such as combination frequencies involving f_r, f_{n1}, and f_{n2} (the second-mode whirl/whip frequency), and stable regions increase compared with those under the first loading condition.

(3) The phenomena about the first- and second-mode whips measured by experiment qualitatively agree with the simulated results, such as the appearance of the second-mode whip and combination frequencies about f_r, f_{n1}, and f_{n2} under the second loading condition. However, simulation and experiment cannot be completely consistent, and because there are some differences between the simulation and the experiment, for instance, the bearing clearance deviation, residual unbalance of the discs, the rubbing between the journal and bearing, changing lubricant viscosity due to the temperature rise, etc.

Acknowledgments We are grateful to the Program for New Century Excellent Talents in University (Grant No. NCET-11-0078) for providing financial support for this work.

Appendix A

$$\boldsymbol{q} = [x_1, \theta_{y1}, x_2, \theta_{y2}, x_3, \theta_{y3}, x_4, \theta_{y4}, x_5, \theta_{y5}, y_1, \theta_{x1}, y_2, \theta_{x2}, y_3, \theta_{x3}, y_4, \theta_{x4}, y_5, \theta_{x5}]^{\mathrm{T}}, \tag{A.1}$$

where x_i, y_i, θ_{xi}, and θ_{yi} ($i = 1, 2, 3, 4, 5$) shown in Fig. 1b are the displacements in x and y directions and angles of orientation associated with the x and y axes,respectively.

$$\boldsymbol{M} = \begin{bmatrix} \boldsymbol{M}_x & 0 \\ 0 & \boldsymbol{M}_y \end{bmatrix}, \quad \boldsymbol{M}_x = \boldsymbol{M}_y = \operatorname{diag}\left[m_1, J_{d1}, m_2, J_{d2}, m_3, J_{d3}, m_4, J_{d4}, m_5, J_{d5}\right], \tag{A.2}$$

$$\boldsymbol{G} = \omega \boldsymbol{J} = \omega \begin{bmatrix} 0 & \boldsymbol{J}_1 \\ -\boldsymbol{J}_1^{\mathrm{T}} & 0 \end{bmatrix}, \quad \boldsymbol{J}_1 = \operatorname{diag}[0, J_{p1}, 0, J_{p2}, 0, J_{p3}, 0, J_{p4}, 0, J_{p5}], \tag{A.3}$$

here J_{pi} and $J_{di}\,(i = 1, 2 \ldots 5)$ are the polar mass moment of inertia and the diametral moment of inertia, respectively.

$$\boldsymbol{K} = \begin{bmatrix} \boldsymbol{K}_x & 0 \\ 0 & \boldsymbol{K}_y \end{bmatrix}, \tag{A.4}$$

$$\boldsymbol{K}_x = \begin{bmatrix}
k_{11} & k_{12} & k_{13} & k_{14} & 0 & 0 & 0 & 0 & 0 & 0 \\
k_{12} & k_{22} & k_{23} & k_{24} & 0 & 0 & 0 & 0 & 0 & 0 \\
k_{13} & k_{23} & k_{33} + k_{blx} & k_{34} & k_{35} & k_{36} & 0 & 0 & 0 & 0 \\
k_{14} & k_{24} & k_{34} & k_{44} & k_{45} & k_{46} & 0 & 0 & 0 & 0 \\
0 & 0 & k_{35} & k_{45} & k_{55} & k_{56} & k_{57} & k_{58} & 0 & 0 \\
0 & 0 & k_{36} & k_{46} & k_{56} & k_{66} & k_{67} & k_{68} & 0 & 0 \\
0 & 0 & 0 & 0 & k_{57} & k_{67} & k_{77} & k_{78} & k_{79} & k_{7,10} \\
0 & 0 & 0 & 0 & k_{58} & k_{68} & k_{78} & k_{88} & k_{89} & k_{8,10} \\
0 & 0 & 0 & 0 & 0 & 0 & k_{79} & k_{89} & k_{99} & k_{9,10} \\
0 & 0 & 0 & 0 & 0 & 0 & k_{7,10} & k_{8,10} & k_{9,10} & k_{10,10}
\end{bmatrix}, \tag{A.5}$$

$$\boldsymbol{K}_y = \begin{bmatrix}
k_{11} & -k_{12} & k_{13} & -k_{14} & 0 & 0 & 0 & 0 & 0 & 0 \\
-k_{12} & k_{22} & -k_{23} & k_{24} & 0 & 0 & 0 & 0 & 0 & 0 \\
k_{13} & -k_{23} & k_{33} + k_{bly} & -k_{34} & k_{35} & -k_{36} & 0 & 0 & 0 & 0 \\
-k_{14} & k_{24} & -k_{34} & k_{44} & -k_{45} & k_{46} & 0 & 0 & 0 & 0 \\
0 & 0 & k_{35} & -k_{45} & k_{55} & -k_{56} & k_{57} & -k_{58} & 0 & 0 \\
0 & 0 & -k_{36} & k_{46} & -k_{56} & k_{66} & -k_{67} & k_{68} & 0 & 0 \\
0 & 0 & 0 & 0 & k_{57} & -k_{67} & k_{77} & -k_{78} & k_{79} & -k_{7,10} \\
0 & 0 & 0 & 0 & -k_{58} & k_{68} & -k_{78} & k_{88} & -k_{89} & k_{8,10} \\
0 & 0 & 0 & 0 & 0 & 0 & k_{79} & -k_{89} & k_{99} & -k_{9,10} \\
0 & 0 & 0 & 0 & 0 & 0 & -k_{7,10} & k_{8,10} & -k_{9,10} & k_{10,10}
\end{bmatrix}. \tag{A.6}$$

The matrix elements of $\boldsymbol{K}_x$ and $\boldsymbol{K}_y$ are as follows:

$$\begin{cases} k_{11} = a_{11} \\ k_{12} = a_{21} \\ k_{13} = -a_{11} \\ k_{14} = a_{21} \end{cases}, \quad \begin{cases} k_{22} = l_1 a_{21} - a_{31} \\ k_{23} = -a_{21} \\ k_{24} = a_{31} \end{cases}, \quad \begin{cases} k_{33} = a_{11} + a_{12} \\ k_{34} = -a_{21} + a_{22} \\ k_{35} = -a_{12} \\ k_{36} = a_{22} \end{cases}, \quad \begin{cases} k_{44} = l_1 a_{21} - a_{31} + l_2 a_{22} - a_{32} \\ k_{45} = -a_{22} \\ k_{46} = a_{32} \end{cases}, \quad \begin{cases} k_{55} = a_{12} + a_{13} \\ k_{56} = -a_{22} + a_{23} \\ k_{57} = -a_{13} \\ k_{58} = a_{23} \end{cases},$$

$$\begin{cases} k_{66} = l_2 a_{22} - a_{32} + l_3 a_{23} - a_{33} \\ k_{67} = -a_{23} \\ k_{68} = a_{33} \end{cases}, \quad \begin{cases} k_{77} = a_{13} + a_{14} \\ k_{78} = -a_{23} + a_{24} \\ k_{79} = -a_{14} \\ k_{7,10} = a_{24} \end{cases}, \quad \begin{cases} k_{88} = l_3 a_{23} - a_{33} + l_4 a_{24} - a_{34} \\ k_{89} = -a_{24} \\ k_{8,10} = a_{34} \end{cases}, \quad \begin{cases} k_{99} = a_{14} \\ k_{9,10} = -a_{24} \\ k_{10,10} = l_4 a_{24} - a_{34} \end{cases},$$

where k_{blx} and k_{bly} denote the stiffnesses of the left bearing in x and y directions, respectively. And

$$\begin{cases} a_{1i} = \frac{12EI}{l_i^3} \\ a_{2i} = \frac{1}{2} l_i a_{1i}, \quad i = 1, 2, 3, 4 \\ a_{3i} = \frac{1}{6} l_i^2 a_{1i} \end{cases}, \tag{A.7}$$

in which E, l_i, and I are the Young's modulus, the distance between every two adjacent lumped mass points, and the area moment of inertia, respectively.

$$\boldsymbol{C} = \boldsymbol{C}_1 + \boldsymbol{C}_2, \tag{A.8}$$

In practical engineering, most structures are multiple-degree-of-freedom systems, whose dampings are mostly assumed by Rayleigh damping theory; namely, the damping matrix is obtained by superposition of mass matrix and stiffness matrix. This simulation method of energy dissipation has a lot of numerical advantages, and it can meet the needs of general structure dynamic analysis. In this paper, Rayleigh damping form is applied to determine the viscous part ($\boldsymbol{C}_1$) of the total damping matrix ($\boldsymbol{C}$), which can be obtained by the following formula [47]:

$$\boldsymbol{C}_1 = \alpha \boldsymbol{M} + \beta \boldsymbol{K}, \tag{A.9}$$

$$\alpha = \frac{60\,(\omega_{n2}\xi_1 - \omega_{n1}\xi_2)\,\omega_{n1}\omega_{n2}}{\pi(\omega_{n2}^2 - \omega_{n1}^2)}, \quad \beta = \frac{\pi\,(\omega_{n2}\xi_2 - \omega_{n1}\xi_1)}{15(\omega_{n2}^2 - \omega_{n1}^2)}, \tag{A.10}$$

where ω_{n1} and ω_{n2} are the first and second order natural frequencies (rev/min); ξ_1 and ξ_2 are the first and second order modal damping ratios, respectively.

$$\boldsymbol{C}_2 = \mathrm{diag}[0, 0, c_{blx}, 0, 0, 0, 0, 0, 0, 0, 0, 0, c_{bly}, 0, 0, 0, 0, 0, 0, 0], \tag{A.11}$$

in which c_{blx} and c_{bly} are the dampings of the left bearing in x and y directions, respectively.

References

1. Muszynska, A.: Rotordynamics. Taylor & Francis, New York (2005)
2. Ding, Q., Zhang, K.P.: Order reduction and nonlinear behaviors of a continuous rotor system. Nonlinear Dyn. **67**, 251–262 (2012)
3. Newkirk, B.L., Taylor, H.D.: Shaft whipping due to oil action in journal bearings. Gen. Electr. Rev. **28**, 559–568 (1925)
4. Rao, J.S.: History of Rotating Machinery Dynamics. Springer, Berlin (2011)
5. Robertson, D.: XII. Whirling of a journal in a sleeve bearing, The London, Edinburgh, and Dublin. Philos. Mag. J. Sci. **15**, 113–130 (1933)
6. Pinkus, O., Sternlicht, B.: Theory of Hydrodynamic Lubrication. McGraw-Hill, New York (1961)
7. Morrison, D., Paterson, A.N.: Paper 14: criteria for unstable oil-whirl of flexible rotors. In: Proceedings of the Institution of Mechanical Engineers Conference Proceedings, vol. 179, pp. 45–55, Sage (1964)
8. Lund, J.W.: Stability and damped critical speeds of a lexible rotor in fluid-film bearings. J. Eng. Ind. **96**, 509–517 (1974)
9. Botman, M.: Experiments on oil-film dampers for turbo machinery. ASME J. Eng. Power **98**, 393–400 (1976)
10. Ehrich, F.F.: A state of the art survey in rotor dynamics-nonlinear and self-excited vibration phenomena. In: Proceedings of the Second International Symposium on Transport Phenomena, Dynamics, and Design of Rotating Machinery Part II, pp. 3–25, Hemisphere Pub. Co. (1988)
11. Nikolajsen, J.L., Holmes, R.: Investigation of squeeze-film isolators for the vibration control of a flexible rotor. ASME J. Mech. Eng. Sci. **21**, 247–252 (1979)
12. Muszynska, A.: Whirl and whip—rotor/bearing stability problems. J. Sound Vib. **110**, 443–462 (1986)
13. Muszynska, A.: Stability of whirl and whip in rotor/bearing systems. J. Sound Vib. **127**, 49–64 (1988)
14. Childs, D., Moes, H., van Leeuwen, H.: Journal bearing impedance descriptions for rotordynamic applications. J. Lubrif. Technol. **99**, 198–210 (1977)
15. Muszynska, A., Bently, D.E.: Anti-swirl arrangements prevent rotor/seal instability. ASME J. Vib. Acoust. Stress Reliab. Des. **111**, 156–162 (1989)
16. Mohan, S., Hahn, E.J.: Design of squeeze film damper supports for rigid rotors. J. Eng. Ind. **96**, 976–982 (1974)
17. Ocvirk, F.W.: Short-Bearing Approximation for Full Journal Bearings. National Advisory Committee for Aeronautics, TN 2808 (1952)
18. Capone, G.: Orbital motions of rigid symmetric rotor supported on journal bearings. La Meccanica Italiana **199**, 37–46 (1986)
19. Capone, G.: Analytical description of fluid-dynamic force field in cylindrical journal bearing. L'Energia Elettrica **3**, 105–110 (1991); (in Italian)
20. Zhang, W., Xu, X.: Modeling of nonlinear oil-film force acting on a journal with unsteady motion and nonlinear instability analysis under the model. Int. J. Nonlinear Sci. Numer. Simul. **1**, 179–186 (2000)
21. Adiletta, G., Guido, A.R., Rossi, C.: Nonlinear dynamics of a rigid unbalanced rotor in journal bearings. Part I: theoretical analysis. Nonlinear Dyn. **14**, 57–87 (1997)
22. Jing, J.P., Meng, G., Sun, Y. et al.: On the non-linear dynamic behavior of a rotor-bearing system. J. Sound Vib. **274**, 1031–1044 (2004)
23. Jing, J.P., Meng, G., Sun, Y. et al.: On the oil-whipping of a rotor-bearing system by a continuum model. Appl. Math. Model. **29**, 461–475 (2005)
24. de Castro, H.F., Cavalca, K.L., Nordmann, R.: Whirl and whip instabilities in rotor-bearing system considering a nonlinear force model. J. Sound Vib. **317**, 273–293 (2008)
25. Ding, Q., Leung, A.Y.T.: Numerical and experimental investigations on flexible multi-bearing rotor dynamics. ASME J. Vib. Acoust. **127**, 408–415 (2005)
26. Cheng, M., Meng, G., Jing, J.P.: Numerical study of a rotor-bearing-seal system. Proc. Inst. Mech. Eng. Part C: J. Mech. Eng. Sci. **221**, 779–788 (2007)
27. Rao, T.V.V.L.N., Biswas, S., Hirani, H. et al.: An analytical approach to evaluate dynamic coefficients and nonlinear transient analysis of a hydrodynamic journal bearing. Tribol. Trans. **43**, 109–115 (2000)
28. Chen, C.L., Yau, H.T.: Chaos in the imbalance response of a flexible rotor supported by oil film bearings with non-linear suspension. Nonlinear Dyn. **16**, 71–90 (1998)
29. Vance, J.M.: Rotordynamics of Turbomachinery. Wiley, New York (1988)
30. Schweizer, B., Sievert, M.: Nonlinear oscillations of automotive turbocharger turbines. J. Sound Vib. **321**, 955–975 (2009)
31. Zhao, X.J., He, H., Xu, S.Y.: Influence of the floating-ring bearing parameters on stability of turbocharge rotor-bearing system. In: The 4th International Symposium on Fluid Machinery and Fluid Engineering, pp. 421-425, No. 4ISFMFE.Ch17, Beijing, China (2008)
32. Gunter, E.J., Chen, W.J.: DyRoBeS-Dynamics of Rotor Bearing Systems User's Manual. RODYN Vibration Analysis, Inc., Charlottesville, VA (2000)
33. Kirk, R.G., Alsaeed, A.A., Gunter, E.J.: Stability analysis of a high-speed automotive turbocharger. Tribol. Trans. **50**, 427–434 (2007)
34. Gunter, E.G., Chen, W.J.: Dynamic analysis of a turbocharger in floating bushing bearings. In: Proceedings of the 3rd International Symposium on Stability Control of Rotating Machinery, Cleveland, OH (2005)
35. Chen, W.J., Gunter, E.J.: Introduction to Dynamics of Rotor-Bearing Systems. Trafford Publishing, Victoria, BC (2005)

36. Tian, L., Wang, W.J., Peng, Z.J.: Effects of bearing outer clearance on the dynamic behaviours of the full floating ring bearing supported turbocharger rotor. Mech. Syst. Signal Process. **31**, 155–175 (2012)
37. Tian, L., Wang, W.J., Peng, Z.J.: Nonlinear effects of unbalance in the rotor-floating ring bearing system of turbochargers. Mech. Syst. Signal Process. **34**, 298–320 (2013)
38. Rao, J.S., Raju, R.J., Reddy, K.V.B.: Experimental investigation on oil whip of flexible rotors. Tribology **3**, 100–103 (1970)
39. Adiletta, G., Guido, A.R., Rossi, C.: Nonlinear dynamics of a rigid unbalanced rotor in journal bearings. Part II: experimental analysis. Nonlinear Dyn. **14**, 157–189 (1997)
40. Fan, C.C., Syu, J.W., Pan, M.C. et al.: Study of start-up vibration response for oil whirl, oil whip and dry whip. Mech. Syst. Signal Process. **25**, 3102–3115 (2011)
41. EI-Shafei, A., Tawfick, S.H., Raafat, M.S. et al.: Some experiments on oil whirl and oil whip. J. Eng. Gas Turbines Power **129**, 144–153 (2007)
42. Sunar, M., Al-Shurafa, A.M.: The effect of disk location, shaft length and imbalance on fluid induced rotor vibrations. Arab. J. Sci. Eng. **36**, 903–918 (2011)
43. Zhong, Y.E., He, Y.Z., Wang, Z., et al.: Rotor Dynamics. Tsinghua University Press, Beijing (1987); (in Chinese)
44. Adiletta, G., Guido, A.R., Rossi, C.: Chaotic motions of a rigid rotor in short journal bearings. Nonlinear Dyn. **10**, 251–269 (1996)
45. Friswell, M.I., Penny, J.E.T., Garvey, S.D., et al.: Dynamics of Rotating Machines, pp. 206–208. Cambridge University Press, Cambridge (2010)
46. Ma, H., Shi, C.Y., Han, Q.K. et al.: Fixed-point rubbing fault characteristic analysis of a rotor system based on contact theory. Mech. Syst. Signal Process. **38**, 137–153 (2013)
47. Bathe, K.J., Wilson, E.L.: Numerical Methods in Finite Element Analysis. Prentice-Hall, New Jersey (1976)